Detection and Tracking of Moving Vehicles with Gotcha Radar Systems

Douglas Page, Gregory Owirka, Howard Nichols[1],

Steven Scarborough, Michael Minardi, LeRoy Gorham[2]

[1]BAE Systems' Technology Solutions, 6 New England Executive Park, Burlington, MA 01803

[2]AFRL/RYA, 2241 Avionics Circle, WPAFB, OH 45433

1. Introduction

The Gotcha radar concept employs a wide antenna beam, along with a high revisit rate and fine radar resolution to allow improved detection, tracking, and identification of ground targets. In an urban environment, radar clutter competing with moving target returns can be very strong, making it difficult to detect a target of interest, distinguish it from false alarms, and perform geolocation and tracking. Moreover, the targets of interest are expected to be maneuvering, which causes defocusing and reduction in amplitude of the target synthetic aperture radar (SAR) image signature [1]. Urban environments are also likely to contain numerous moving targets producing SAR responses in the vicinity of targets being tracked, making mis-associations more likely.

In this paper, we describe an approach for improving detection and geolocation of moving targets in a track extension scenario. Assuming a well-established track has been formed on a target of interest through optical or other means, the goal is to continue to track the target by processing only radar data. This approach employs tracker feedback and a multi-channel Gotcha radar system to address the challenges described above in order to provide improved detection, geolocation, and tracking of a single target of interest. While some of the techniques we describe here may also be applicable to wide-area ground moving target indication (GMTI), the approach as a whole is based on using tracker feedback and localized processing to improve performance. Consequently it is less applicable to wide-area GMTI, because the number of false associations and false alarms over a wide area may negatively impact the benefits of tracker feedback.

One challenge for performing GMTI with Gotcha radar systems is that moving targets may be competing with stationary clutter over a wide area spanned by the antenna footprint. Deming [2] has studied application of displaced phase-center antenna (DPCA) and along-track interferometry (ATI) for performing GMTI in Gotcha radar systems. In our approach, we employ space-time adaptive processing (STAP) [3,4], which tailors an adaptive filter to a local clutter environment and to the parameters of a target of interest in order to maximize the signal to interference plus noise ratio (SINR) for improved detection performance. Additionally, moving target SAR defocus is compensated for in our approach using a technique known as moving reference processing (MRP). The original formulation of MRP [1] reprocesses phase history data in order to produce a focused response from a moving target having known motion parameters. We employ a more efficient form of MRP that operates on a localized chip after polar format SAR image formation has been performed. After STAP and MRP is performed, a noncoherent form of SAR change detection is employed which reduces false alarms due to clutter discretes. Employment of a "tracker in the loop" reduces the SAR-MRP search space, and separates targets of interest from other movers while refining geolocation of the target.

As background, Section 2 briefly describes a method for detecting movers in SAR data that pre-dated the approach described in this paper. Section 3 describes the general scatterer model underlying our SAR moving target processing. The effects of Doppler shift, SAR defocus, and compensation for defocus using MRP are discussed. A simulated example of a moving target in point clutter is also presented, demonstrating theoretical validity of our formulation. Section 4 describes a combination of MRP and STAP to raise moving targets above the clutter and obtain maximum likelihood parameter estimates. Results for the SINR loss factor in our simulated vehicle example are presented as a function of the clutter-to-noise ratio (CNR) of the clutter scatterer. In addition to showing simulated SINR loss of our STAP/MRP implementation, for comparison we also show the simulated performance of several other more standard implementations. In Section 5, we illustrate detection, false alarm mitigation, and parameter

estimation during tracker-in-the-loop processing. Results at different stages of the processing for real CPI examples are shown in order to illustrate the processing as well as demonstrate how well it works. Section 6 gives a brief summary of the paper and Section 7 provides the list of references.

2. Addressing Slow Movers with SAR-MRP

It is well known that moving targets within a standard SAR imaging scene are defocused, displaced, or completely missing in the final image. AFRL has conducted prior research on the focusing of moving targets in SAR imagery, resulting in an algorithm called SAR Moving Reference Processing (SAR-MRP) [1]. This algorithm focuses and geolocates moving targets by reprocessing the SAR data to focus the movers rather than the stationary clutter. SAR change detection is used so that target detection and focusing is performed more robustly. Combining the advantages of persistent-stare continuous-dwell SAR with the moving-target focusing from SAR-MRP offers the potential to detect and track moving targets at fine SAR resolutions and high update rates. If data from multiple passes is combined coherently, a zero Minimum Detectable Velocity (MDV) is possible, provided that the interference is very well correlated across the passes (when interference is not as well correlated across passes, benefits can still be seen using noncoherent change detection methods).

As considered here, the SAR-MRP approach phase shifts each pulse of the SAR data equivalent to the motion of the moving reference. Once the moving reference has been applied, standard image formation techniques can be used. If target motion is not known, which is generally the case, a number of motion hypotheses are applied and the hypothesis generating the “best” target focus is selected as most likely to match actual target motion. This search over all plausible target motion states is clearly the biggest challenge to a useful implementation of SAR-MRP. Not only is there a large computational cost to searching over plausible motions in three dimensions, but selecting the best hypothesis can produce many false alarms in the presence of stationary objects. The latter is true because, as will be illustrated with a simulated example in

Section 4, applying MRP will in general defocus the responses from stationary objects, and the defocused responses from different objects can produce interference and false peaks.

3. Scatterer SAR/MRP Model

3.1 *General Model*

Figure 1 illustrates the collection geometry for a multi-channel spotlight SAR scenario. We consider a model for the radar motion-compensated phase history of an isotropic moving point scatterer. The radar platform is assumed to transmit from a time-dependent location $\vec{\mathbf{r}}_X(t)$, where t is the slow-time or pulse time. The radar platform is assumed to have a number of receive-antenna channels with locations $\vec{\mathbf{r}}_R(n,t)$ where the index n labels the different channels. The target scatterer has a time-dependent location given by $\vec{\mathbf{r}}_{sc}(t)$.

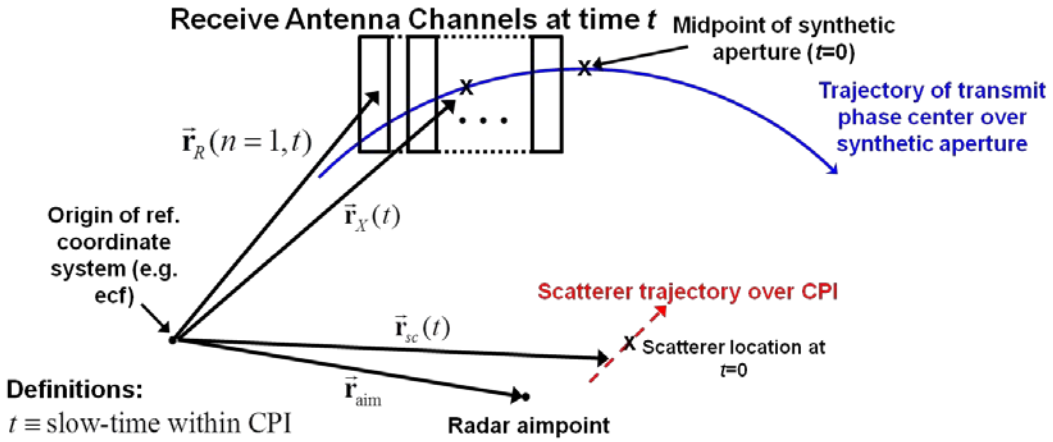

Figure 1 Definition of quantities appearing in scatterer model

Our processing operates on a complex phase history $P(\lambda,t)$ as a function of wavelength and slow time (or pulse). Assuming a constant target radar cross section (RCS) and far-field

propagation, our model for the motion-compensated phase history of a moving point scatterer is given by

$$P_{sc}(n,\lambda,t) = A_{sc} \cdot \exp\{-j \cdot \frac{2\pi}{\lambda} \cdot [|\vec{\mathbf{r}}_X(t) - \vec{\mathbf{r}}_{sc}(t)| + |\vec{\mathbf{r}}_R(n,t) - \vec{\mathbf{r}}_{sc}(t)| - C(n,t)]\} \quad (1)$$

Motion compensation has also been assumed to have been performed (compensation term shown as $C(n,t)$). The parameter A_{sc} represents the complex scatterer amplitude, which due to the isotropic scatterer assumption is assumed independent of slow-time and receive channel.

In a general imaging situation, there will be radar returns from stationary scatterers, moving targets, and thermal noise. In order to form a focused SAR image of a stationary scene around the radar aimpoint, a polar formatting procedure is employed that performs a mapping from wavelength and slow-time to a 2-D k-space. Defining a polar angle $\theta(t)$ as the angle of the platform line of sight projected into the slant plane, we have

$$\begin{gathered} \mathbf{k}_y(\lambda,t) = \frac{4\pi}{\lambda}\cos\theta(t), \quad \mathbf{k}_x(\lambda,t) = \frac{4\pi}{\lambda}\sin\theta(t) \\ k(\lambda) \equiv \sqrt{\mathbf{k}_x(\lambda,t)^2 + \mathbf{k}_y(\lambda,t)^2} \end{gathered} \quad (2)$$

The polar format transformation (2) can be inverted to obtain wavelength and slow time as functions of $\mathbf{k}_x$ and $\mathbf{k}_y$. Denoting these two functions by $\lambda(\mathbf{k}_x,\mathbf{k}_y)$ and $t(\mathbf{k}_x,\mathbf{k}_y)$ respectively, a radar phase history function $P(n,\lambda,t)$ produces a corresponding phase history function on two-dimensional k-space:

$$\tilde{P}(n,\mathbf{k}_x,\mathbf{k}_y) \equiv P(n,\lambda(\mathbf{k}_x,\mathbf{k}_y),t(\mathbf{k}_x,\mathbf{k}_y)) \quad (3)$$

Typically, a two-dimensional rectangular grid in k-space is defined, and the values of the function $\tilde{P}(n,\mathbf{k}_x,\mathbf{k}_y)$ in Eq. (3) are obtained using a two-dimensional interpolation into the input phase history $P(n,\lambda,t)$. SAR image formation can then be accomplished by performing a two-dimensional discrete Fourier transform. Defining x_{im}, y_{im} as the output location within the SAR image, we have the following equation for the polar format SAR images in each antenna channel:

$$Q(n, x_{im}, y_{im}) = \sum_{\mathbf{k}_x=\mathbf{k}_{x,\min}}^{\mathbf{k}_x=\mathbf{k}_{x,\max}} \sum_{\mathbf{k}_y=\mathbf{k}_{y,\min}}^{\mathbf{k}_y=\mathbf{k}_{y,\max}} \exp\{-j\cdot[\mathbf{k}_x \cdot x_{im} + \mathbf{k}_y \cdot y_{im}]\} \cdot \tilde{P}(n, \mathbf{k}_x, \mathbf{k}_y) \tag{4}$$

3.2 Constant acceleration model for MRP

For a general target motion, the phase of $\tilde{P}(n, \mathbf{k}_x, \mathbf{k}_y)$ is not linear in k-space, but has k-dependent terms that produce a defocus when 2-D Fourier transform SAR image formation shown in Eq. (4) is performed. If the target motion is known, one can compensate for the defocus using MRP [1]. The original formulation of MRP processes phase history data prior to polar format image formation (i.e. across slow-time and fast-frequency or wavelength). If the scatterer motion is known, however, one can alternatively introduce an MRP focus function $M(F, \mathbf{k}_x, \mathbf{k}_y)$ to compensate for defocus terms on polar-formatted data as follows:

$$Q(n, F, x_{im}, y_{im}) = \sum_{\mathbf{k}_x=\mathbf{k}_{x,\min}}^{\mathbf{k}_x=\mathbf{k}_{x,\max}} \sum_{\mathbf{k}_y=\mathbf{k}_{y,\min}}^{\mathbf{k}_y=\mathbf{k}_{y,\max}} \exp\{-j\cdot[\mathbf{k}_x \cdot x_{im} + \mathbf{k}_y \cdot y_{im}]\} \cdot M(F, \mathbf{k}_x, \mathbf{k}_y) \cdot \tilde{P}(n, \mathbf{k}_x, \mathbf{k}_y) \tag{5}$$

Here, we have introduced a symbol *F* as representing a derived target MRP motion parameter or set of parameters which specify the focus function required for a desired class of target motion models. The number of elements of *F* and the equations specifying the elements depend on the nature of the scatterer motion.

To illustrate SAR defocus and compensation using MRP, we consider a target moving with acceleration, having the following location versus time characteristic:
constant

$$\vec{\mathbf{r}}_{sc}(t) = \vec{\mathbf{r}}_{sc}(0) + \vec{\mathbf{v}}_{sc}(0)\cdot t + \frac{1}{2}\vec{\mathbf{a}}_{sc}(0)\cdot t^2$$
$$\vec{\mathbf{r}}_{sc}(0) \equiv \text{scatterer location (3D vector) at mid-aperture}$$
$$\vec{\mathbf{v}}_{sc}(0) \equiv \text{scatterer velocity vector (3D) at mid-aperture} \tag{6}$$
$$t \equiv \text{slow-time across CPI (defined to be 0 at mid-aperture)}$$
$$\vec{\mathbf{a}}_{sc}(0) \equiv \text{scatterer acceleration vector (3D) at mid-aperture}$$

The scatterer motion for a constant acceleration model is thus seen to be quadratic in slow-time across the CPI. Through Taylor's theorem, for reasonable platform motions and short enough CPI length the phase in Eq. (1) will also be well-approximated by a quadratic function of t (as determined by expanding the phase function in a second order Taylor series with respect to t). The latter approximation in turn leads, through the transformation shown in Eq. (3), to a specific form of the MRP focus function $M(F, \mathbf{k}_x, \mathbf{k}_y)$ that effectively focuses up the target response.

Figure 2 shows simulated SAR responses before and after MRP for two different scatterers: a slowly moving but accelerating point target (representing a vehicle) and a stationary point clutter scatterer. The upper left subfigure in Figure 2 shows that before MRP, the target response is defocused. Note that in the range dimension, the target response is concentrated mainly in 2 range pixels, while in the cross-range dimension it is concentrated over about 45 pixels. The lower left subfigure shows that the clutter scatterer is completely focused in a single pixel before MRP. This is expected, as the simulated clutter point scatterer location was selected to place it in the center of a pixel after polar format SAR image formation, and the SAR imaging filter is designed to focus up stationary point scatterers.

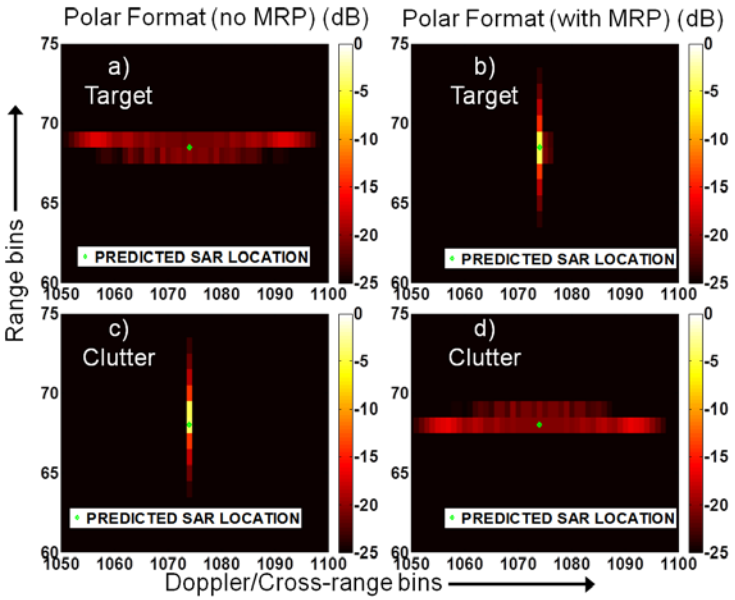

Figure 2 Simulated MRP example: image responses of a slowly moving accelerating target (upper subfigures) and single stationary point clutter scatterer (lower subfigures). Response are shown before (left subfigures) and after (right subfigures) MRP is applied: a) upper left subfigure shows response of target before MRP b) upper right subfigure shows response of target after MRP c) lower left subfigure shows response of clutter scatterer before MRP d) lower right subfigure shows response of clutter scatterer after MRP. Green diamond shows predicted SAR locations based on the known scatterer parameters.

The upper right subfigure in Figure 2 shows that applying MRP using Eq. (5) based on the scatterer model (6) focuses the target response along the cross-range dimension, with the energy being essentially contained within one cross-range column. Along the range dimension, the energy is still seen to be primarily contained within two range pixels. The reason that the target is not completely focused in range is that there is an offset between the center of a range pixel and the mean target range over the CPI. In other words, the MRP filter has corrected for a time variation of target range over the CPI, but not for the offset between the center of a range pixel and the mean target range. The behavior along range is similar to the response of a point scatterer straddling two range bins: significant response seen in two adjacent range bins, with a range sidelobe response that is characteristic of the SAR imaging filter.

The lower right subfigure in Figure 2 shows that applying MRP defocuses the response of the clutter scatterer along cross-range, while not affecting the response along range. Again this behavior is expected, as the MRP filter is designed to focus a moving target having a particular time-dependent range vs. time characteristic. When this filter is applied to data from a stationary scatterer, it will introduce time dependent terms that produce defocus along the cross-range dimension.

The predicted image locations of the responses of the two scatterers can be derived by expanding the phase of the function shown in Eq. (3) in a first order Taylor series with respect to $\mathbf{k}_x$ and $\mathbf{k}_y$. The predicted x and y image locations are then obtained from the estimated slopes of the phase function with respect to $\mathbf{k}_x$ and $\mathbf{k}_y$ respectively. The predicted locations are shown as

green diamonds in Figure 2, and are seen to be in agreement with the observed locations of the responses.

4. Combination of MRP and STAP to Raise Moving Targets Above Clutter

4.1 MRP search procedure

The above simulation example used the calculated parameters of the simulated target to perform MRP. When processing measured data and tracking an actual vehicle, we need to search over the MRP parameters to account for uncertainty in our knowledge of the vehicle motion state, as well as to accommodate time variation of the motion state. The resulting complex chips for each processed set of MRP parameters (including the "zero" parameter set F_0 corresponding to no MRP) are stored in a multi-dimensional array which is sent to the STAP part of the processing, which will allow moving targets to be separated from the clutter returns. The dimensions of the multi-dimensional MRP output array include: range index, cross-range index, antenna channel index, and indices into the MRP parameter set F.

4.2 STAP filtering

STAP [3,4] is an effective technique for detecting targets in strong interference with multi-channel, pulse-Doppler radars. In order to perform STAP, we must first select a set of adaptive degrees of freedom (DOFs). Standard factored post-Doppler STAP [4] forms adaptive spatial beamform weights across the antenna channels in each Doppler bin. This allows tailoring of adaptive filters to match local clutter statistics, but performance is limited by the selection of spatial-only adaptive DOFs. To improve adapted target/clutter performance of post-Doppler STAP, adaptive temporal DOFs can be added [4] by creating time-staggered sub-CPIs (the so-called "PRI-staggered" approach) or by stacking data from adjacent Doppler bins (the "extended factored" or "adjacent Doppler bin" post-Doppler approach). Here we qualitatively describe a different set of temporal DOFs tailored to the SAR-GMTI problem.

To improve the ability to separate targets and clutter in a given SAR pixel, adaptive DOFs can be created as follows:

$$\vec{\mathbf{d}}(x_{im}, y_{im}) = \begin{bmatrix} Q(1, F_0, x_{im}, y_{im}) \\ Q(2, F_0, x_{im}, y_{im}) \\ \vdots \\ Q(N_n, F_0, x_{im}, y_{im}) \\ Q(1, F_1, x_{im}, y_{im}) \\ Q(2, F_1, x_{im}, y_{im}) \\ \vdots \\ Q(N_n, F_1, x_{im}, y_{im}) \\ \vdots \\ Q(N_n, F_{N_F-1}, x_{im}, y_{im}) \end{bmatrix} \tag{7}$$

Here, we stack the data for different channels (n) and different MRP parameter sets ($\{F_k$, $k=0,1,\ldots N_F\text{-}1\}$) in each pixel. Figure 2 showed how the responses of a moving target and a clutter scatterer change when MRP is performed. Basically, a moving target will increase in amplitude and focus up, while a stationary clutter scatterer will go down in amplitude and defocus when MRP is applied using a set of parameters F corresponding to the location, velocity, and acceleration of the moving target. The goal is to select DOFs shown in Eq. (7) that minimize the overlap of the target and clutter response vectors.

Once the adaptive DOFs have been defined, calculation of the adaptive matched filter (AMF) [5] can be performed in order to cancel the clutter, perform detection, and obtain maximum likelihood (ML) parameter estimates [6]. The formula for calculating the AMF uses an estimated covariance matrix $\mathbf{R}$ (defined over the adaptive DOF set). In post-Doppler STAP, training data for the estimated covariance matrix is obtained using data vectors from different range pixels in the same cross-range (pseudo-Doppler) column as the pixel under test. In order to reduce target contamination of the covariance estimates, we exclude the test pixel from the training data. The equation defining the covariance estimate is:

$$\mathbf{R}(x, y) = \frac{1}{N_{y'}} \sum_{y' \neq y} \vec{\mathbf{d}}(x, y') \vec{\mathbf{d}}(x, y')^H \tag{8}$$

The sum is over range pixels (y') in the same cross-range column (x) as the test cell, but excluding the test range cell (y). Each term in the sum (8) is an outer product of a data vector with its Hermitian conjugate (indicated using the "H" superscript). The sum is normalized by dividing by the number of training pixels. Eq. (8) gives a maximum likelihood estimate of the covariance matrix, assuming uniform (i.e. homogeneous) clutter statistics over the training window [4]. In order to produce a "good" covariance estimate, the number of training pixels should be a multiple of the rank of the true covariance. For full-rank interference, the required number of training pixels is therefore a multiple of $N_n * N_F$ (number of DOFs in Eq. (7)). For full-rank homogeneous Gaussian interference, a factor of 2 (i.e. number of training pixels = twice the number of DOFs) gives a "training loss" factor of 3 dB. In practice, one desires a factor greater than two to allow for non-Gaussian clutter statistics and to produce a smaller training loss.

In addition to an estimated covariance matrix, the equation for the STAP AMF also uses a steering vector $\vec{\mathbf{s}}(\beta)$, which may depend on one or more parameters (collectively represented as β). The steering vector represents a possible target response across the adaptive DOF set. For SAR-GMTI processing, a bank of steering vectors can be formed corresponding to different values of angle of arrival (AOA) and MRP motion state parameters (i.e., β is a vector parameter set containing AOA and the elements of the MRP parameter set F). A search is performed over the parameters β in order to obtain maximum likelihood estimates, as will be shown below. Each steering vector will have the same number of elements as the data vector shown in Eq. (7). The elements themselves will have a far-field phase progression across the N_n antenna channels depending on the assumed target AOA and the antenna channel phase center locations. Additionally there will be an amplitude and phase progression across the N_F MRP DOFs depending on the target motion model assumed.

The equation for the parameter-dependent AMF in a pixel (x,y) is given by

$$AMF(\beta, x, y) = \frac{|\vec{\mathbf{s}}(\beta)^H \mathbf{R}(x,y)^{-1} \vec{\mathbf{d}}(x,y)|^2}{\vec{\mathbf{s}}(\beta)^H \mathbf{R}(x,y)^{-1} \vec{\mathbf{s}}(\beta)} \quad (9)$$

The AMF is known to have an embedded constant false alarm rate (CFAR) property [5]. Detection is performed in each pixel by comparing the AMF, maximized over the target parameters, with a specified detection threshold:

$$\max_{\beta} AMF(\beta, x, y) >= T \quad (10)$$

In addition to having a CFAR property, the AMF also acts as a ML parameter estimator [6]. For SAR-GMTI processing, this means that ML estimates of AOA and MRP motion state can be obtained as the corresponding parameter values that maximize the AMF:

$$\hat{\beta}(x, y) = \arg\max_{\beta} AMF(\beta, x, y) \quad (11)$$

Note that while parameter estimates could be obtained in each pixel, these estimates are only used in pixels for which the maximum AMF exceeds the detection threshold.

4.3 SINR Loss for different STAP configurations in a simulated example

Figure 3 shows the effect of employing different adaptive DOFs on the output SINR after STAP (relative to a matched filter in thermal noise) for the simulated example shown in Figure 2, as a function of the CNR of the clutter scatterer. For reference, the SINR curves for non-adaptive conventional processing across the antenna channels before ("Conv.", black curve) and after ("Non-adaptive MRP", magenta curve) MRP are also shown. The conventional results were obtained by using antenna channel DOFs only (i.e. using Eq. (7) with N_F=1), and a covariance matrix proportional to the identity matrix in Eq. (9) (i.e. a known covariance assuming thermal noise interference). The red curve ("STAP (no MRP)") corresponds to employing post-Doppler "factored" STAP (i.e. using only adaptive antenna spatial DOFs in each Doppler filter, no temporal DOFs) before MRP (i.e. using Eq. (7) with N_F=1), but using an adaptively estimated covariance as shown in Eq. (8). The green curve corresponds to employing factored STAP using the same spatial-only DOFs after performing MRP.

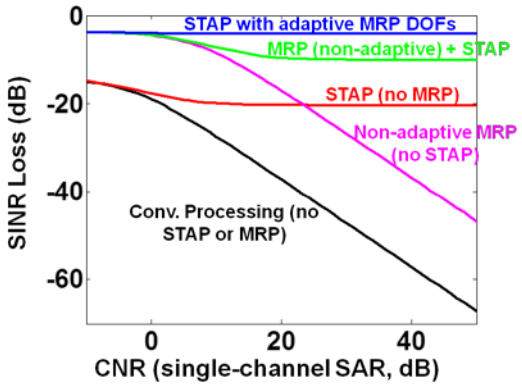

Figure 3 SINR Loss vs. CNR for simulated constant acceleration MRP example

The difference between the black and red curves thus shows the SINR improvement if factored STAP is used instead of conventional beamforming across the antenna channels, without any MRP. Observe that the red curve levels off as the CNR increases, indicating that the STAP filter is effectively nulling the clutter. Applying MRP nonadaptively raises the target SNR and improves the performance of conventional beamforming. This is seen in Figure 3 by looking at the change from the black to magenta curves. However, note that the magenta SINR drops off strongly with increasing CNR, indicating that STAP is needed. Applying MRP is also seen to improve the performance of factored STAP further (red to green curves). The blue curve corresponds to an implementation of post-Doppler STAP with spatial antenna DOFs and temporal MRP DOFs as shown in Eq. (7) with N_F>1, and using an adaptively estimated covariance matrix as shown in Eq. (8). Observe that the blue curve clearly provides the best SINR in this simulated example. While this example may be a simplified case, it does contain the essential elements of the real situation. Note that the results in this section apply to single-pass or multi-pass data, and no change detection was used to produce the results (in our approach change detection is only used for false alarm mitigation).

5. Detection, False Alarm Mitigation, and Parameter Estimation on Measured Radar Data

5.1 Results for actual CPI example #1

Figure 4 shows the imaging geometry, and single channel SAR target chip for an example containing a vehicle visible in the single-channel SAR image (i.e. an "easy" example). The (Doppler-shifted) truth location is also shown on the chip, and the horizontal green lines on the right half of Figure 4 show the detection search box (i.e. the area over which detection processing is performed). The actual chip extracted is larger than the detection search box in order to give more training data for both image registration (to the reference orbit) and covariance estimation (for STAP).

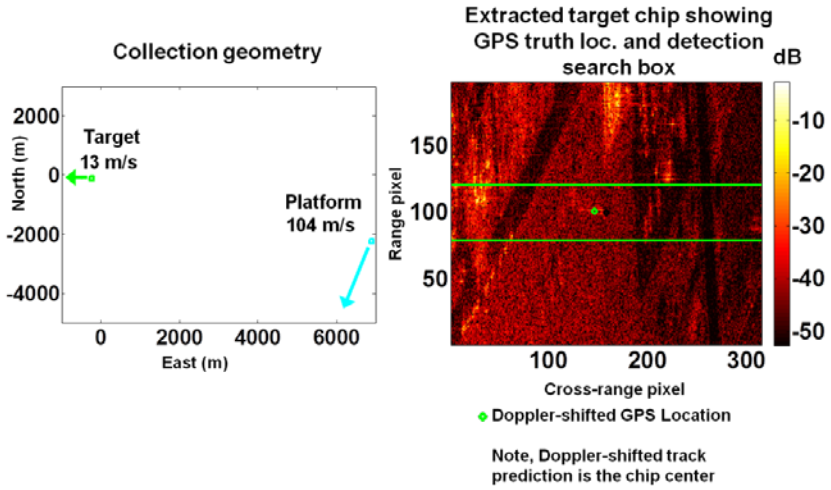

Figure 4 Imaging geometry (left) and extracted SAR chip (right) for an "easy" CPI; a vehicle visible in the image

Note that this CPI came from a tracking run, so that the center of the chip is defined by the location and velocity of the mean track state, which is then converted to SAR image coordinates. The size of the detection search box is a function of the track covariance matrix, which is enlarged to allow for fixed systematic errors, possible radial acceleration, and expected cross-range defocus. This localized processing allows lower detection thresholds than would be the

case for a wide-area GMTI mode, because the chances of a false alarm over the processed portion are smaller for a localized chip than for a large image.

As mentioned in the introduction, in order to reduce the chances of updating the tracker with a false alarm or detection from a target other than the vehicle under track, a number of additional false alarm mitigation steps are performed. One of these steps is a noncoherent form of change detection which we refer to as Object Level Change Detection (OLCD). Our processing assumes that two orbits of data from the radar platform are available. In addition to the "mission" pass SAR image containing the vehicle of interest, a "reference" pass image from a previous platform orbit is also processed on each CPI. This processing results in two corresponding AMF images. Figure 5 shows the maximum AMF images over the detection search box for both mission and reference orbits on the processed CPI that was shown in Figure 4.

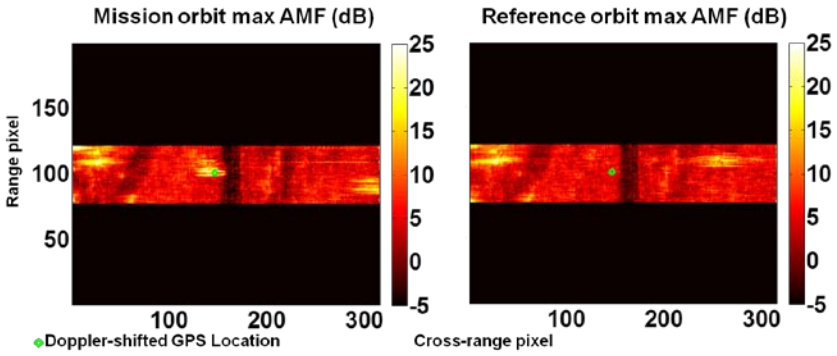

Figure 5 STAP Maximum AMF images for mission and reference orbits for example shown in previous figure

We expect the target of interest to appear near the indicated GPS truth location in the mission AMF image but not the reference AMF image (note: the truth is not used in any of the processing, only for evaluation purposes). Note that Figure 5 is showing AMF images that are maximized over the steering vector parameters (i.e. AOA and MRP motion state) in each pixel. Due to the effect of MRP on clutter (Figure 2), we expect any residual clutter to be defocused. Additionally, as we are searching over a grid of defocus parameters, we also expect the target AMF response to be defocused, due to MRP cross-range sidelobes.

To extract detections from the maximum AMF images, we first perform a thresholding of the mission orbit AMF image using Eq. (10). The set of potential target detections is next reduced by applying OLCD. The OLCD step reduces false alarms due to clutter that are undernulled by the STAP filter (due, for example, to covariance estimation errors caused by spatially varying clutter amplitude). Such false alarms should be seen in both mission and reference orbit STAP AMF images.

In order to perform further false alarm mitigation and also to perform geolocation, we carry out a measurement of the so-called "clutter ridge." The clutter ridge specifies channel-to-channel phase shift across the receive antenna phase centers as a function of cross-range pixel. The channel-to-channel phase shift is in turn related to AOA. For the current example, ambiguities (multiple branches) exist due to the fact that the antenna spacing is greater than half a wavelength.

Figure 6 shows the mission orbit STAP AMF image after thresholding and OLCD, along with the set of detections remaining after false alarm mitigation for the CPI example that was shown in Figure 4 and Figure 5. The right half of Figure 6 shows the AOA index of the detections as a function of cross-range along with the measured clutter ridge. Note that in addition to the Doppler-shifted GPS location (green diamond), the "true" GPS location (i.e. without Doppler shift) is also indicated (green square). For each remaining detection passing the false alarm mitigation step, geolocation is next performed. The first step in geolocating a given detection is to determine the cross-range pixel for which the clutter ridge AOA index matches the estimated AOA index of the detection. More simply, a horizontal line is drawn from the detection to determine where it intersects the clutter ridge (blue arrow in plot on right half of Figure 6). Even after applying the steps described above to reduce the set of possible target detections, there may still be detections from multiple scatterers in the processed search area. In fact, Figure 6 shows detections occurring in two well-separated portions, likely coming from two different targets. In order to further decrease the chances of mis-association and improve time in track on the vehicle

of interest, we select a single detection on each CPI that correlates the best with the reference track state. The blue "x" on the right half of the right subfigure in Figure 6 shows the Doppler-shifted location of the detection that was selected on that CPI. The blue square on the left half of the right subfigure shows the corresponding "true" location after AOA estimation and geolocation. On this CPI, the selected detection was seen to be fairly close to the center of the chip in the left subfigure in Figure 6 (which in turn is the same as the Doppler-shifted track location).

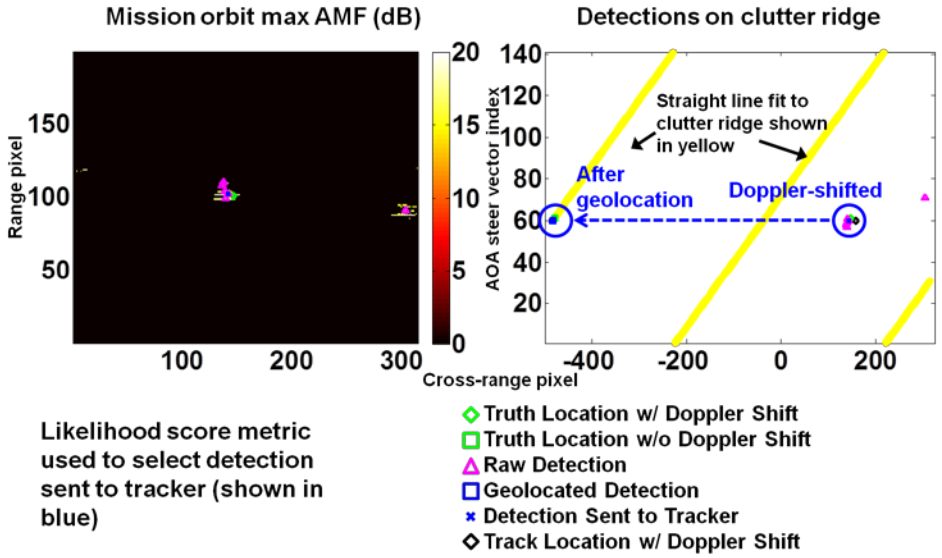

Figure 6 STAP AMF Image after OLCD and thresholding (left plot), and detections after thresholding and false alarm mitigation (right plot)

As an indicator of detection and geolocation performance on this CPI example, one can compare the location of the final selected detection with the location of the GPS truth. A comparison of the Doppler-shifted locations (blue x vs. green diamond) near the center of the left subfigure in Figure 6, and on the right half of the right subfigure in Figure 6, shows that the selected detection is close to the GPS location in both range and cross-range (the black diamond on the right half of the right subfigure also shows the Doppler-shifted track location). A comparison of the blue square vs. green square on the left half of right subfigure in Figure 6 also shows that the AOA (vertical axis) of the selected detection, is also close to the AOA of the GPS

truth. The measured AOA corresponds to a particular "true" cross-range location on the clutter ridge, which is also seen to be close to the GPS location (horizontal axis). On this CPI, the fact that the target is close to the GPS truth in 3 independent measurements (range, cross-range, and AOA) increases the confidence that we are detecting the vehicle of interest and estimating its parameters accurately. We reiterate here that the truth is used only for evaluation purposes and is not used in any way to select the detection; only the track information is used.

Figure 7 shows a zoomed portion of the single-channel SAR image before and after MRP, using the estimated MRP parameter set associated with the detection that was sent to the tracker in the above example. Observe the improved focus and amplitude of the target response, demonstrating the validity of our MRP model on actual measured data. The fact that the target response can be seen, even after applying MRP, indicates that this CPI is a relatively benign case where the target has plenty of RCS to raise it above the clutter returns that it is Doppler shifted over. We now turn to an example of a more challenging CPI from the same tracking run.

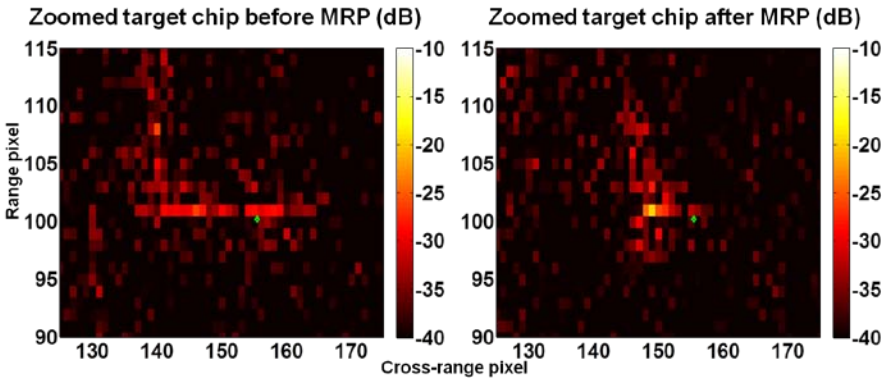

Figure 7 Zoomed portion of chip containing target before and after MRP

5.2 Results for actual CPI example #2

Figure 8 shows the SAR imaging geometry and extracted chip for one of the antenna channels on a different CPI from the same vehicle tracking run. As will be seen, on this CPI detection is more challenging than for the previous example. Figure 9 shows that the target response is close to some strong residual clutter that is appearing in both mission and reference orbit AMF images. The residual clutter seen in Figure 9 occurs due to undernulling, which results when the pixel

under test contains stronger clutter than the training window used to estimate the covariance matrix. Figure 10 shows that after the additional steps of thresholding and false alarm mitigation, only detections from the vehicle of interest remain. The selected detection is again seen to be close to the GPS truth location in the 3 measured coordinates (range, cross-range, and AOA). Additionally, the Doppler-shifted and true locations of the track (shown as a black diamond and a black square respectively in Figure 10) are seen to be close to the corresponding GPS truth coordinates, indicating that the tracking accuracy is good at this point in the tracking run.

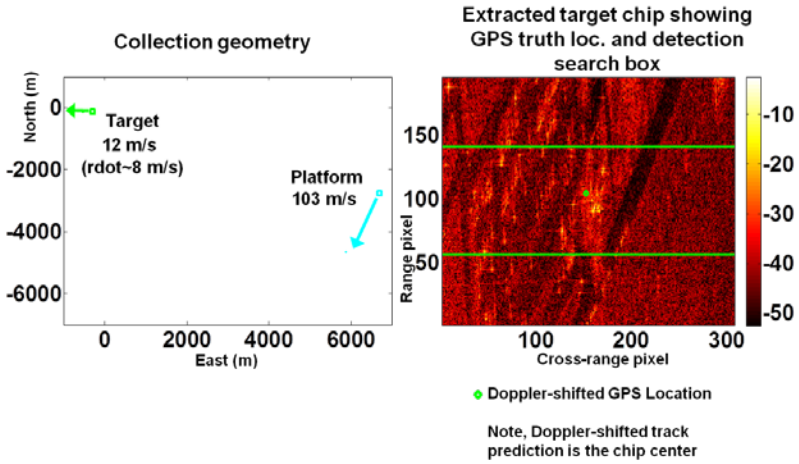

Figure 8 Extracted SAR chip and imaging geometry for a more challenging vehicle CPI

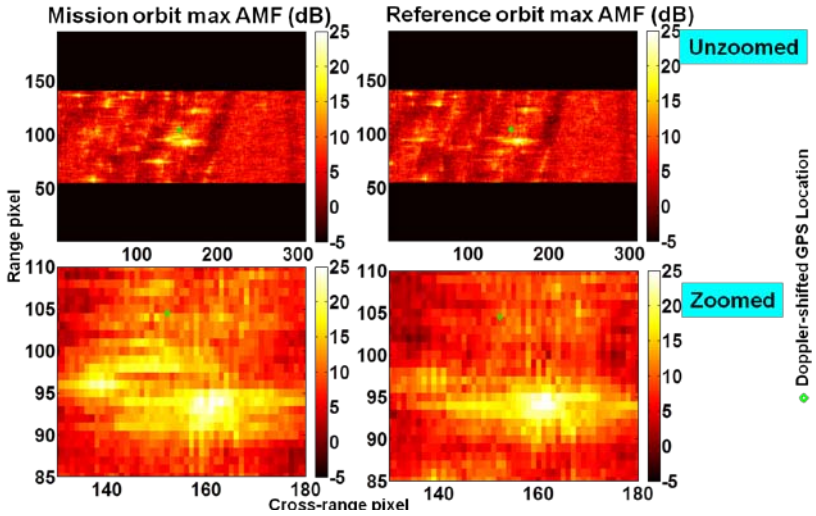

Figure 9 STAP Maximum AMF image for mission (left) and reference (right) passes

While we have focused on detecting a single target of interest, some of the techniques we have described are also applicable to wide area GMTI. In particular, the STAP formulation described in Section 4 can be applied to wide area processing. However, the effectiveness of the adaptive MRP DOFs will depend on how well the target motion states used to perform MRP match the targets under surveillance. In a wide area scenario, it will be more difficult to obtain accurate motion state estimates than in a single-target scenario. Consequently, the realized benefits of our approach may not be nearly as great when applied to wide area GMTI surveillance. Additionally, the computation burden of performing covariance estimates and applying MRP filters can become significant over a large surveillance area.

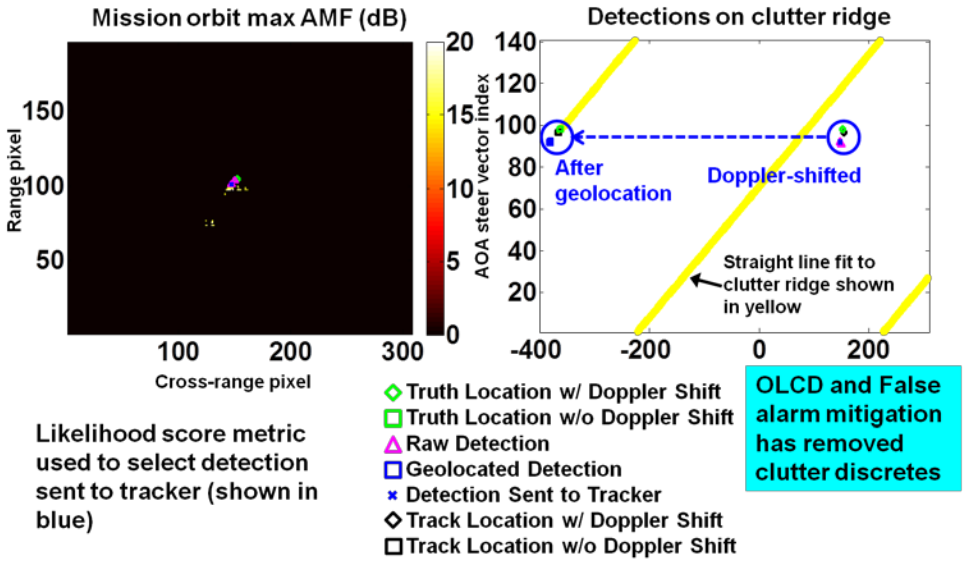

Figure 10 STAP AMF Image after OLCD and thresholding (left) and detections after thresholding and false alarm mitigation (right)

6. Summary and Conclusions

In summary, we have defined an approach for detecting and tracking moving vehicles with Gotcha radar systems. Our approach exploits tracker-feedback to address challenges for detection, false alarm mitigation, geolocation and tracking in an urban surveillance environment. We presented a mathematical framework for processing multi-channel SAR data in order to mitigate the combined effects of moving target defocus and strong clutter interference. Our

algorithm uses MRP adaptively in a STAP framework to focus up moving vehicles and enhance signal to clutter ratios. Using simulated data, we illustrated SAR defocus of an accelerating point scatterer and mitigation of the defocus using MRP. For this simulated example, we also presented the potential improvements to SINR loss using our adaptive processing compared to more standard STAP approaches.

A number of techniques have also been discussed to extract detections, mitigate false alarms, and minimize the chances of mis-association. The performance of these techniques were demonstrated qualitatively using sample CPIs from a multi-channel airborne radar tracking run. Comparison to the truth showed that MRP effectively focused up the moving-target response on a CPI in which the target was visible in the single-channel SAR imagery and was not competing with strong clutter. A second CPI example was also presented in which the target was not visible in the single-channel SAR imagery and strong clutter was present near the Doppler-shifted truth location. Using our adaptive processing and false alarm mitigation processing was demonstrated to provide detection of the moving target and allow accurate location of the target close to the truth.

7. References

[1] S. Scarborough, C. Lemanski, H. Nichols, G. Owirka, M. Minardi, T. Hale, “SAR Change Detection MTI,” Algorithms for Synthetic Aperture Radar Imagery XIII, Edmund G. Zelnio, editor, Proceedings of SPIE, 2006.

[2] R. Deming, S. MacIntosh, M. Best, "Three-channel processing for improved geo-location performance in SAR-based GMTI interferometry”, Proc. SPIE. 8394, 83940F (2012).

[3] I. S. Reed, J. D. Mallett, and L. E. Brennan, “Rapid convergence rate in adaptive arrays,” IEEE Trans. Aerospace Elec. Sys., Vol. 10 No. 6, pp. 853-863 (Nov. 1974).

[4] J. Ward, “Space-Time Adaptive Processing for Airborne Radar,” Tech. Rep. F19628-95-C-0002, MIT Lincoln Laboratory, December 1994

[5] Frank C. Robey, Daniel R. Fuhrmann, Edward J. Kelly, Ramon Nitzberg, "A CFAR Adaptive Matched Filter Detector," IEEE Transactions on Aerospace and Electronic Systems, Vol. 28, pp. 208-216, (1992)

[6] James Ward, "Angle and Doppler Estimation with STAP Radar," 4th Annual Adaptive Sensor Array Processing (ASAP) Workshop, 14 March 1996